

# Multi-physics Model and Optimization of a Solenoid Valve

by

**Kutlay Hanlı**

A Dissertation Submitted to the  
Graduate School of Sciences and Engineering  
in Partial Fulfillment of the Requirements for  
the Degree of

Master of Science

in

Mechanical Engineering



**KOÇ ÜNİVERSİTESİ**

December 19, 2022

## Multi-physics Model and Optimization of a Solenoid Valve

Koç University

Graduate School of Sciences and Engineering

This is to certify that I have examined this copy of a master's thesis by

**Kutlay Hanlı**

and have found that it is complete and satisfactory in all respects,  
and that any and all revisions required by the final  
examining committee have been made.

Committee Members:

---

Assoc. Prof. Arif Karabeyoğlu (Advisor)

---

Prof. Metin Muradoğlu

---

Prof. Onur Tuncer

Date: \_\_\_\_\_

# **ABSTRACT**

## **Multi-physics Model and Optimization of a Solenoid Valve**

**Kutlay Hanlı**

**Master of Science in Mechanical Engineering**

**December 19, 2022**

There are several limitations when designing solenoid systems. With proper search space selection possible designs can be narrowed down lightest, fastest and most power efficient depending on the application. A method was developed starting from computing required coil design to overcome sealing forces, minimizing structural thicknesses to reduce weight and looking into the effect of manufacturing tolerances and clearances as a perturbation matrix. This was achieved by a multi-physics simulation where the magnetic circuit is modeled using magnetic reluctances of parts and clearances. The fluid flow was computed assuming ideal gas, 1D flow and adiabatic process.

# ÖZETÇE

## Solenoid Vana Çoklu-fizik Modeli ve Optimizasyonu

Kutlay Hanlı

Makine Mühendisliği, Yüksek Lisans

19 Aralık 2022

Solenoid sistemleri tasarlarken birçok kısıtlama vardır. Doğru tarama alanı ile olası tasarımlar en hafif, en hızlı ve en verimli olarak ayıklanabilir. Bobinin yenmesi gereken kuvvete göre bobin tasarlayarak başlayan, sonrasında ağırlığı azaltmak için yapısal kalınlıkları azaltan, üretim toleransları ve boşlukların etkisini hesaplayan bir model geliştirilmiştir. Bu model bir çoklu fizik modelidir, parça ve boşlukların relüktansını hesaplamaktadır. Akış hesaplamaları da ideal gaz, 1 boyutlu akış ve adyabatik süreç varsayımlarıyla hesaplanmıştır.

## ACKNOWLEDGMENTS

I would like to express my gratitude to my supervisor Assoc. Prof. Arif Karabeyoğlu for their continuous support. I wish to show my appreciation to DeltaV engineers and close friends Murat Çetinkaya, Recep Ufuk and Utku Can Yıldız for their support in developing and testing our models in DeltaV facilities.

## TABLE OF CONTENTS

<b>List of Figures</b>	<b>viii</b>
<b>Abbreviations</b>	<b>xi</b>
<b>Chapter 1: Magneto Motive Force</b>	<b>1</b>
1.1 Magnetic Flux . . . . .	1
1.1.1 Magnetic Reluctance . . . . .	1
1.1.2 $N \cdot I$ (Ampere Turns) . . . . .	6
1.2 Armature Surface Area . . . . .	7
<b>Chapter 2: Magnetic Model of a Solenoid Valve</b>	<b>10</b>
<b>Chapter 3: Dynamic Model of a Solenoid Valve</b>	<b>15</b>
3.1 Mechanical Model . . . . .	15
3.2 Electrical Model . . . . .	16
3.3 Simulation Meta Data . . . . .	18
3.4 Flow Model . . . . .	18
3.4.1 Armature Motion . . . . .	19
3.4.2 Electrical and Magnetic Circuit Simulation . . . . .	19
3.4.3 Control Volume Changes . . . . .	20
3.4.4 Gas Flows . . . . .	20
<b>Chapter 4: Simulation</b>	<b>23</b>
<b>Chapter 5: Conclusion</b>	<b>31</b>
5.1 Optimizing Coil Parameters . . . . .	31
5.2 The Effect of Structural Elements Thickness . . . . .	34

5.3 The Effect of Clearances and Tolerances . . . . .	36
<b>Bibliography</b>	<b>39</b>
<b>Appendix A:</b>	<b>40</b>

## LIST OF FIGURES

1.1	Magnetic flux through a simple bar . . . . .	2
1.2	The structural schematic of the HSV [Zhao et al., 2017] . . . . .	2
1.3	Comparison between simulated and experimental results of the elec- tromagnetic force [Zhao et al., 2017] . . . . .	3
1.4	Influence of the driving current on the electromagnetic force incre- ment at different working air gaps [Zhao et al., 2017] . . . . .	3
1.5	Influence of driving current on total magnetic reluctance at different working air gaps [Zhao et al., 2017] . . . . .	4
1.6	The B-H curve of the iron core and armature. [Zhao et al., 2017] . . .	5
1.7	Influence of h on the electromagnetic force at different driving currents [Zhao et al., 2017] (x axis is in 10mm) . . . . .	5
1.8	Influence of h on the total magnetic reluctance at different driving currents [Zhao et al., 2017] (x axis is in 10mm) . . . . .	6
1.9	Electromagnetic force of different Ampere-turns [Yang et al., 2019] . .	7
1.10	Traditional micro high-speed digital valve [Yang et al., 2019] . . . . .	8
1.11	Novel micro high-speed digital valve [Yang et al., 2019] . . . . .	9
1.12	Electromagnetic force for different arrangement [Yang et al., 2019] . .	9
2.1	Magnetic path shown on assembly . . . . .	10
2.2	Detail view on vertical air gap between magnetic top and shell. . . . .	11
2.3	Detail view on horizontal air gap between shell and magnetic bottom. . .	12
2.4	Detail view on horizontal air gap between magnetic bottom and ar- mature. . . . .	13
2.5	Detail view on vertical effective air gap between magnetic top and armature. . . . .	13



3.1	Armature Free Body Diagram . . . . .	15
3.2	Schematic of electrical circuit. (left) Valve powered off. (right) Valve powered on. . . . .	16
3.3	(a) An RL circuit with a switch to turn current on and off. When in position 1, the battery, resistor, and inductor are in series and a current is established. In position 2, the battery is removed and the current eventually stops because of energy loss in the resistor. (b) A graph of current growth versus time when the switch is moved to position 1. (c) A graph of current decay when the switch is moved to position 2.[OpenStax, 2022] . . . . .	18
3.4	Abstraction of valve volumes, and flow paths. . . . .	19
4.1	Electrical and magnetic circuit development over time. . . . .	25
4.2	Magnetic field strengths and magnetic flux densities reached during simulation. . . . .	26
4.3	All forces acting on the armature. . . . .	26
4.4	Forces acting on the armature excluding pressure forces. . . . .	27
4.5	Motion on the armature. . . . .	27
4.6	Mass flows to and from control volumes. . . . .	28
4.7	Pressures of control volumes and reservoirs. . . . .	29
4.8	Control volume pressure and temperature . . . . .	29
4.9	Change of the volumes . . . . .	30
4.10	Change of the masses . . . . .	30
5.1	Shortened simulation visualization. Simulation and driving voltage start at $t = 0$ , and driving voltage is removed at the vertical black line. . . . .	32
5.2	Response times of various design options. Trade-offs between opening and closing times. . . . .	33
5.3	x axis represents the time it takes to flow 1 kg of gas during an oscillating valve operation (continuous opening and closing of the valve). . . . .	34

5.4	Results of simulation: Valve Weight and minimum flow per cycle . . .	34
5.5	Response times of various design options. Trade-offs between opening and closing times. . . . .	35
5.6	x axis represents the time it takes to flow 1 kg of gas during an oscillating valve operation (continuous opening and closing of the valve).	36
5.7	Results of simulation: Valve Weight and minimum flow per cycle . . .	36
5.8	The effect of clearances on valve opening and closing times. . . . .	37
5.9	The effect of clearances on valve weight. . . . .	38
5.10	The 3D model of the optimized valve. . . . .	38

## ABBREVIATIONS

$c_a$	Axial clearance
$c_r$	Radial clearance
$h_C$	Coil height
$h_{Cout}$	Coil outer radius
$D_w$	Wire diameter
$t_{cfr}$	Coil former radial thickness
$t_{cfa}$	Coil former axial thickness
$t_{mba}$	Magnetic bottom axial thickness
$t_{mta}$	Magnetic top axial thickness
$t_{shell}$	Shell thickness
$r_A$	Armature radius
$r_{cham}$	Chamfer radius offset
$h_{cham}$	Chamfer height
PR	Solenoid packing ratio
CWCC	Coil wire current capacity
ERC	Electrical resistivity of copper

## Chapter 1

**MAGNETO MOTIVE FORCE**

Magneto motive force is the force that allows solenoid valves to open using the linear motion of an armature. Magneto motive force is a function of magnetic flux  $\phi$ , surface area perpendicular to the magnetic flux acting on armature  $S_2$  and magnetic reluctance of vacuum or material filling range of linear motion  $\mu_0$ .

$$F_{mag} = \frac{1 \cdot \phi^2}{2 \cdot \mu_0 \cdot S_2} \quad (1.1)$$

**1.1 Magnetic Flux**

Magnetic flux through the magnetic circuit of a solenoid valve is a function of coil turns  $N$ , current through the coil  $I$ , and total magnetic reluctance of the magnetic circuit  $R_{total}$ .

$$\phi = \frac{N \cdot I}{R_{total}} \quad (1.2)$$

$N$  is constrained by the geometry of the valve, there is a limit on how many turns one can add for a given cross sectional area.  $I$  is constrained by the wire current carrying capacity. In further sections we will analyze the effect of wire diameter and valve geometry on magnetic flux and magneto motive force.

**1.1.1 Magnetic Reluctance**

Magnetic reluctance  $R$  of a simple 430F stainless steel block can be computed as:

$$R = \frac{l}{\mu_0 \mu_r A} \quad (1.3)$$

where  $l$  is length of the magnetic path in meters,  $\mu_0$  is permeability of free space (vacuum)  $4\pi \cdot 10^{-7} H/m$ ,  $\mu_r$  is relative permeability of a magnetic material (850 for

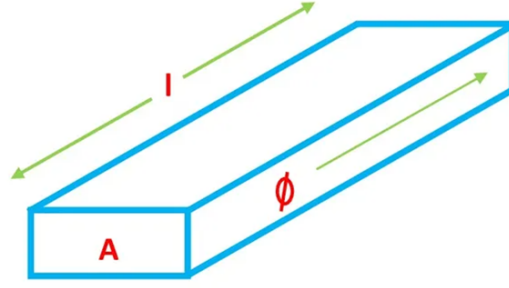


Figure 1.1: Magnetic flux through a simple bar

430F SS) and  $A$  is the cross sectional area in  $m^2$ . [Zhao et al., 2017] Zhao et al. studied the effect of structural parameters of a solenoid system with the model in fig. 1.2.

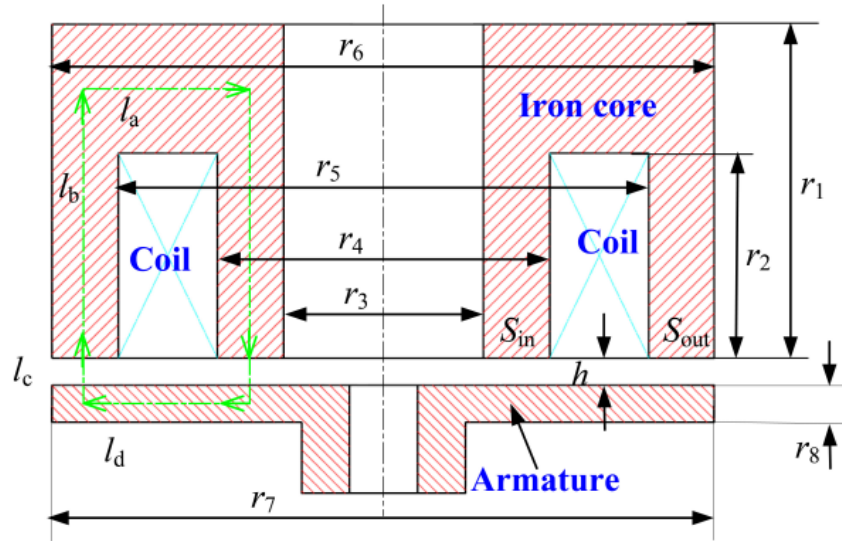


Figure 1.2: The structural schematic of the HSV [Zhao et al., 2017]

Zhao et al. computed the total magnetic reluctance through the green arrows, magnetic circuit path, and computed the magnetic flux and magneto motive force. Researchers validated their static electromagnetic force model by running experiments on a test bench where they fixed the armature and the force sensor at one end and placed the iron core free on the other end 1.3. They present the effects of driving current on electromagnetic energy conversion in fig.

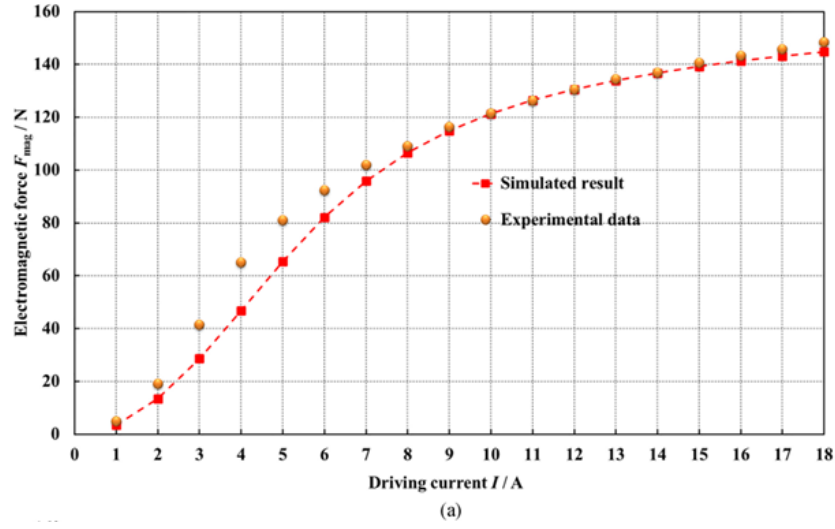


Figure 1.3: Comparison between simulated and experimental results of the electromagnetic force [Zhao et al., 2017]

1.4.

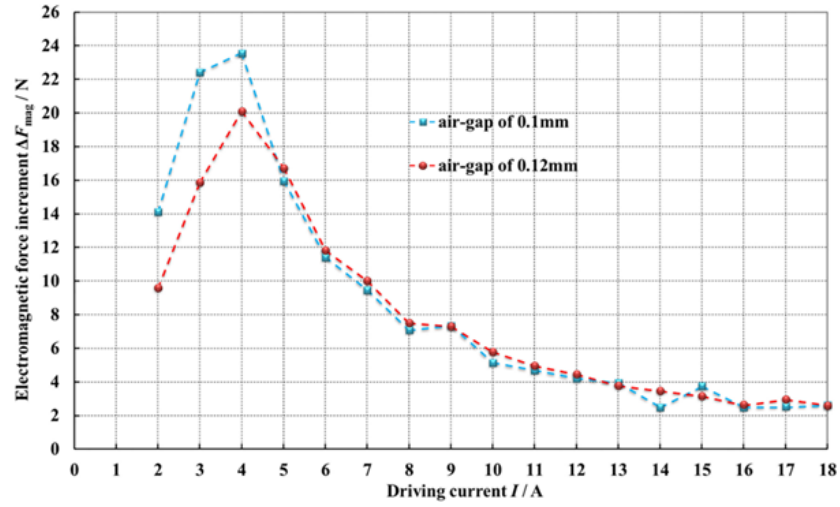


Figure 1.4: Influence of the driving current on the electromagnetic force increment at different working air gaps [Zhao et al., 2017]

“When  $I$  increases from 1A to 18A, the electromagnetic force first increases rapidly,  $\partial F / \partial I$  reaches a maximum value at a driving current of 4A, and then decreases. When  $I < 4A$ , with increasing  $I$ , the increase of the electromagnetic force at the air gap of 0.1mm always greater than that at the air gap of 0.12mm. When

$I > 4A$ , the two curves nearly overlap, and the increment of the electromagnetic force with increasing  $I$  gradually decreases. The phenomena can be explained with the B-H curve of the iron core and armature.” [Zhao et al., 2017]

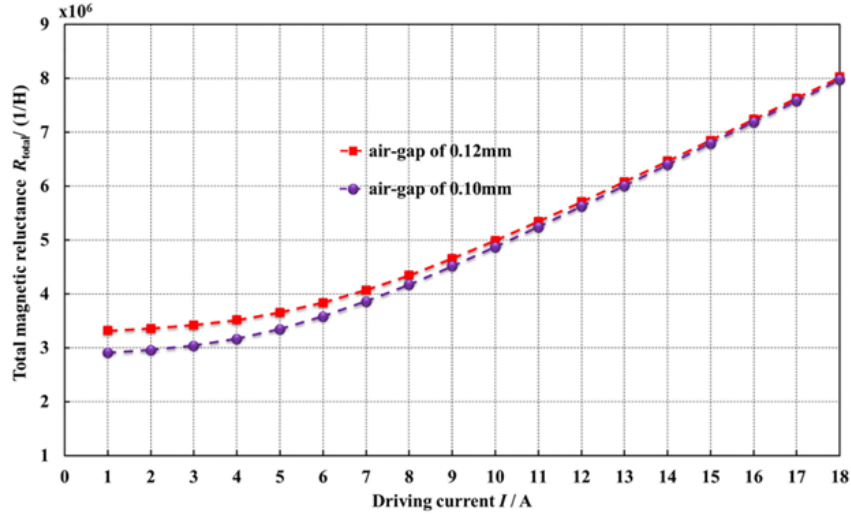


Figure 1.5: Influence of driving current on total magnetic reluctance at different working air gaps [Zhao et al., 2017]

As seen in fig. 1.5, change  $\partial R/\partial I$  starts to dominate the total magnetic reluctance. The researchers conclude that “increasing  $I$  will cause premature saturation in the HSV, and the magnetic reluctance of the soft magnetic material will become a decisive factor in restricting the variation of the total magnetic reluctance, which causes the changes of the total magnetic reluctance at different working air gaps to be the same with increasing  $I$ . Therefore, it can be surmised that when  $I > 4A$ , the electromagnetic forces with different working air gaps will increase at the same rate with increasing  $I$ .” [Zhao et al., 2017]

The fig 1.6 show us the B-H curve and it shows how magnetic saturation occurs. To increase the materials magnetic flux density one must exponentially increase the magnetic field intensity which results in high power consumption or is limited by solenoids current carrying capacity. “ $I$  and the working air gap both have significant effects on the variation of the total magnetic reluctance. Too large current or small working air gap will lead to the saturation of magnetic circuit.” [Zhao et al., 2017] For an efficient solenoid system the air gap should have the highest magnetic reluctance

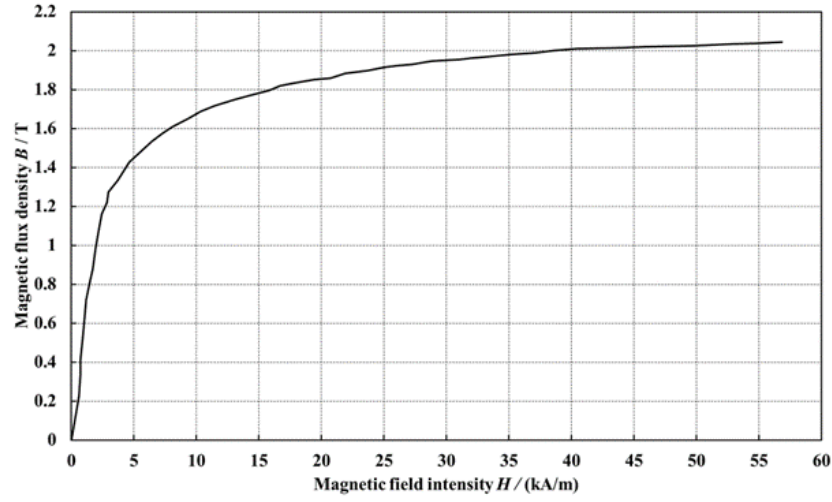


Figure 1.6: The B-H curve of the iron core and armature. [Zhao et al., 2017]

contribution to the total magnetic reluctance.

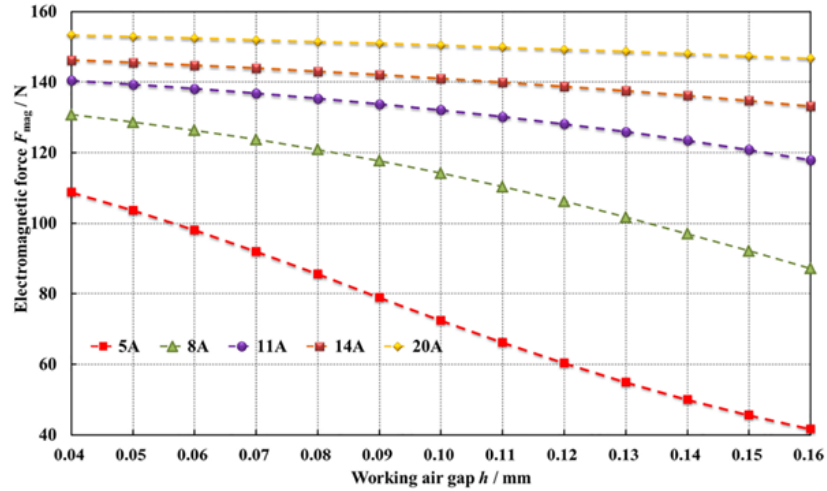


Figure 1.7: Influence of  $h$  on the electromagnetic force at different driving currents [Zhao et al., 2017] (x axis is in 10mm)

“Fig 1.7 shows that at different values of  $I$ , the electromagnetic force decreases with an increasing of the working air gap, and the rate of decrease is affected by the value of  $I$ . The larger  $I$  becomes, the smaller the rate is.” [Zhao et al., 2017] This occurs because the magnetic reluctance caused by saturation dominates the magnetic reluctance due to the air gap.



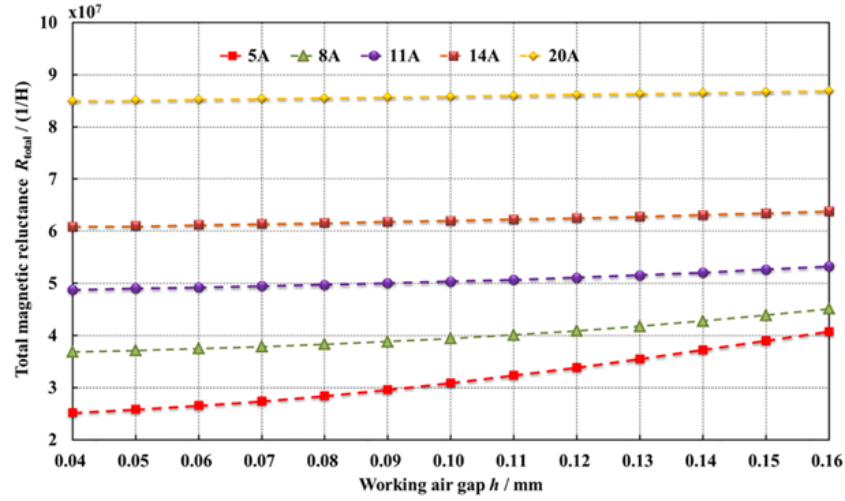


Figure 1.8: Influence of  $h$  on the total magnetic reluctance at different driving currents [Zhao et al., 2017] (x axis is in 10mm)

The fig. 1.8 “shows that at different values of  $I$ , the total magnetic reluctance increases with an increase of the working air gap. When the total magnetic flux is constant, the electromagnetic force decreases with increasing total magnetic reluctance. If  $I$  is small, the capability of electromagnetic energy conversion in the HSV will be significantly influenced by the working air gap. But if  $I$  is large enough to lead to the magnetic saturation, the working air-gap has only a minor influence.” [Zhao et al., 2017]

### 1.1.2 $N \cdot I$ (Ampere Turns)

As seen in eq. 1.1, magneto motive force is linearly proportional to  $N \cdot I$ . There is however a limit to this relationship. In fig. 1.9 Yang et al. shows that magneto motive force is saturated. It should be noted that for different air gaps (range of linear motion) the saturation level varies. Different air gap distances result in exponential increase in air gap magnetic reluctance. Thus it requires more ampere turns to increase the magnetic reluctance of the magnetic circuit to match and exceed the air gap.

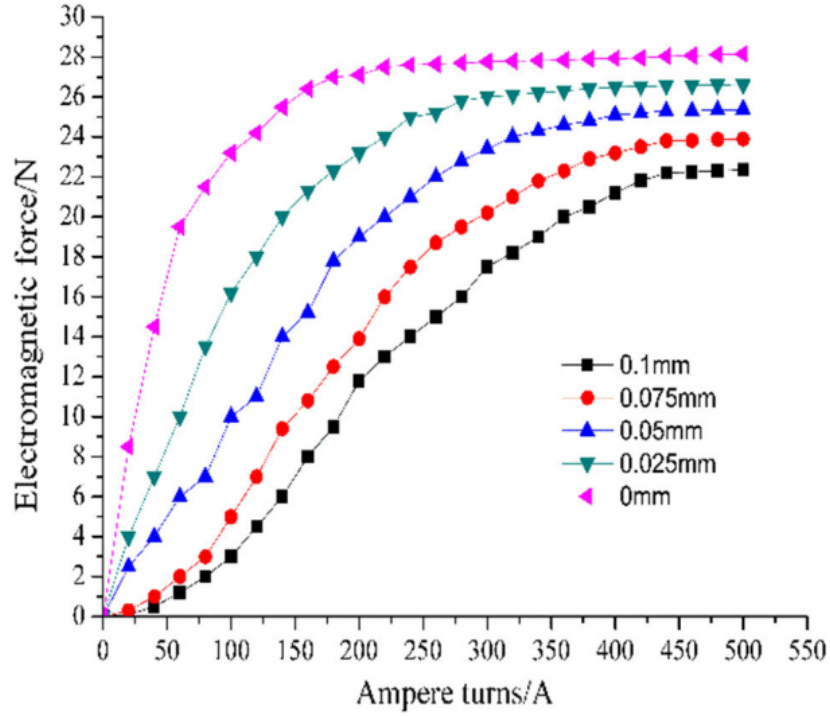


Figure 1.9: Electromagnetic force of different Ampere-turns [Yang et al., 2019]

## 1.2 Armature Surface Area

Armature surface area perpendicular to the magnetic flux acting on it is crucial in determining magneto motive force as seen in eq. 1.1. Yang et al. improved the efficiency of a micro digital valve by changing the design in such a way that they increased the armature surface area which led to an increase in magnetic flux thus increasing the magneto motive force for the same  $N \cdot I$  [Yang et al., 2019].

“Under the same displacement of the iron core, the testing results of electromagnetic force of the novel micro high-speed digital valve were about 1.33 times as that of the traditional valve. ... ratio of the testing results was in good agreement with the area ratio of the two valves.” [Yang et al., 2019]

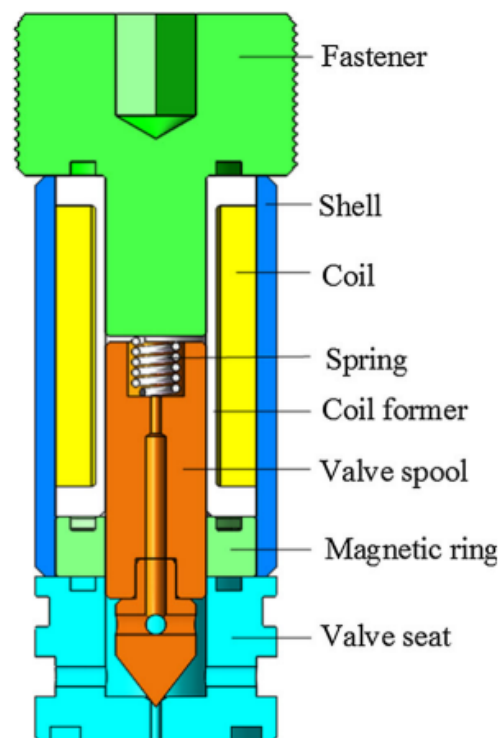


Figure 1.10: Traditional micro high-speed digital valve [Yang et al., 2019]

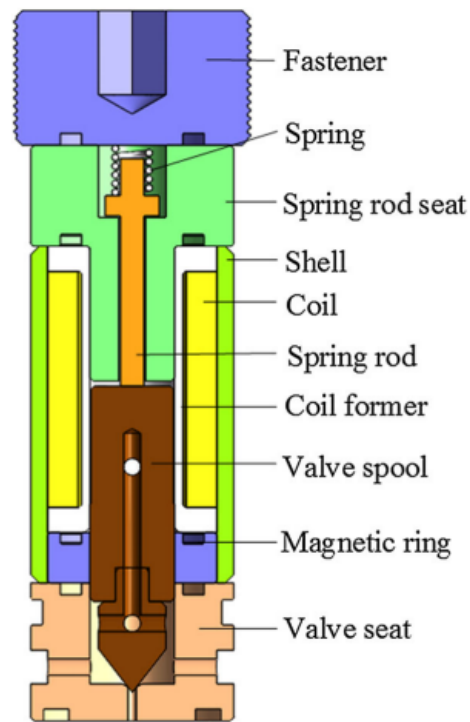


Figure 1.11: Novel micro high-speed digital valve [Yang et al., 2019]

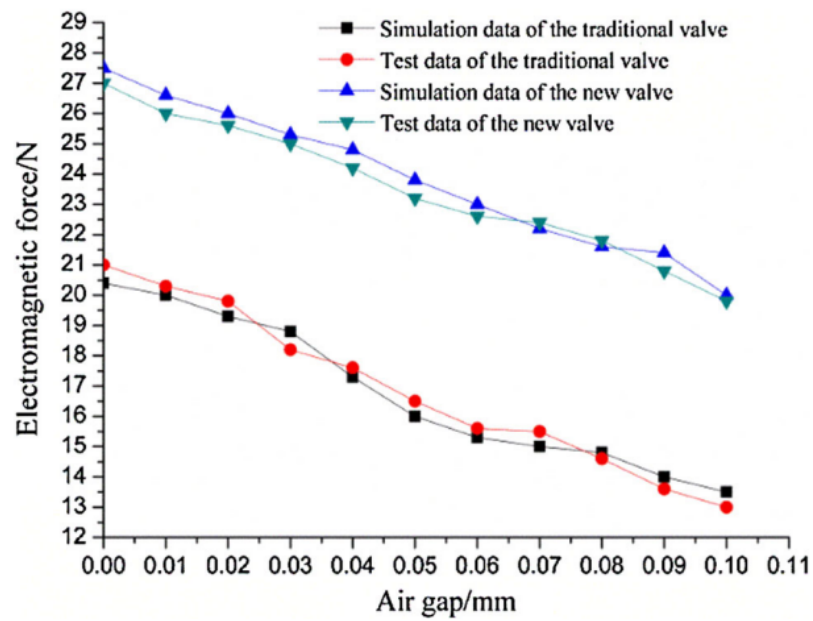


Figure 1.12: Electromagnetic force for different arrangement [Yang et al., 2019]

## Chapter 2

## MAGNETIC MODEL OF A SOLENOID VALVE

In this chapter we will be modelling the magnetic circuit of the HSV by Yang et al. from the previous chapter.

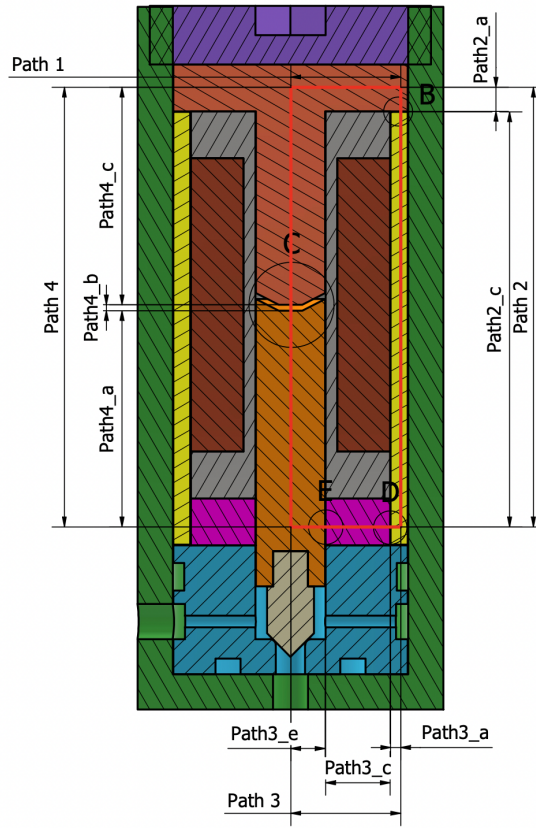


Figure 2.1: Magnetic path shown on assembly

As seen in Fig. 2.1, magnetic circuit is divided into 4 linear sections following the method of Zhao et al. *Path1* is uninterrupted and flows through the part labeled as magnetic top.

$$R_{\text{path1}} = \frac{4 r_{\text{Cout}}}{\mu \mu_0 t_{\text{mta}} \pi (c_a + c_r + 2 r_{\text{Cout}} + t_{\text{shell}})} \quad (2.1)$$

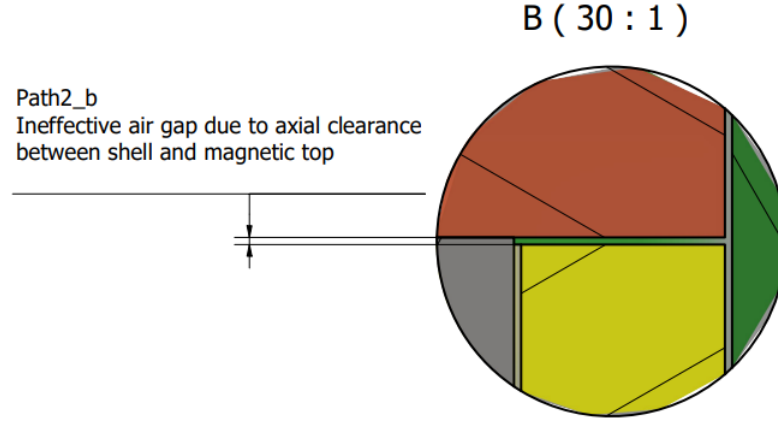


Figure 2.2: Detail view on vertical air gap between magnetic top and shell.

Path 2 is divided into 3 sections.  $Path2_a$  is the outer vertical path through the magnetic top.  $Path2_b$  is the vertical path through the ineffective air gap due to axial clearance between shell and magnetic top shown in Fig. 2.2.  $Path2_c$  is the path through shell.

$$R_{\text{path2}} = \frac{c_a}{\mu_0 \pi ((c_r + r_{\text{Cout}} + t_{\text{shell}})^2 - (c_r + r_{\text{Cout}})^2)} + \frac{h_C - c_a + 2 t_{\text{cfa}} + \frac{t_{\text{mba}}}{2} + t_{\text{mta}}}{\mu \mu_0 \pi ((c_r + r_{\text{Cout}} + t_{\text{shell}})^2 - (c_r + r_{\text{Cout}})^2)} \quad (2.2)$$

Path 3 is divided into 5 sections.  $Path3_a$  is the horizontal path through shell.  $Path3_b$  is the path through ineffective air gap due to radial clearance between shell and magnetic bottom shown in Fig. 2.3.  $Path3_c$  is the horizontal path through magnetic bottom.  $Path3_d$  is the path through ineffective air gap due to radial clearance between shell and magnetic bottom shown in Fig. 2.4.  $Path3_e$  is the horizontal path through the armature.

$$\begin{aligned}
R_{\text{path3}} = & \frac{2}{\mu \mu_0 t_{\text{mba}} \pi} + \\
& \frac{c_r}{\mu_0 t_{\text{mba}} \pi \left( \frac{c_r}{2} + r_A \right)} + \\
& \frac{c_r}{\mu_0 t_{\text{mba}} \pi \left( \frac{c_r}{2} + r_{\text{Cout}} \right)} + \\
& \frac{t_{\text{shell}}}{2 \mu \mu_0 t_{\text{mba}} \pi \left( c_r + r_{\text{Cout}} + \frac{t_{\text{shell}}}{2} \right)} - \\
& \frac{2 (c_r + r_A - r_{\text{Cout}})}{\mu \mu_0 t_{\text{mba}} \pi (c_r + r_A + r_{\text{Cout}})}
\end{aligned} \tag{2.3}$$

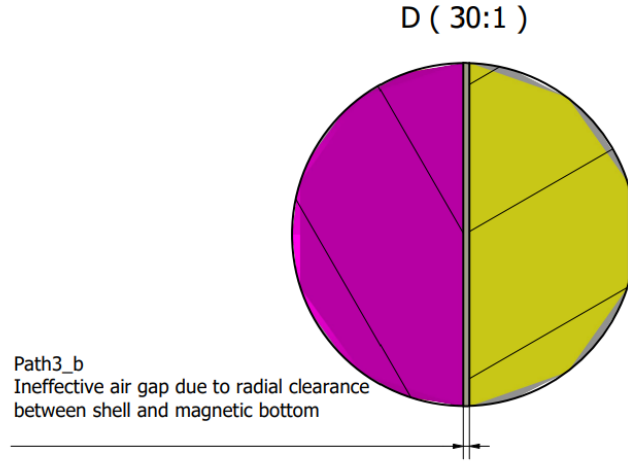


Figure 2.3: Detail view on horizontal air gap between shell and magnetic bottom.

Path 4 is divided into 3 sections.  $Path4_a$  is the vertical path through the armature.  $Path4_b$  is the path through the effective air gap shown in Fig. 2.5 where the use full magneto motive force is generated.  $Path4_c$  is the vertical path through magnetic top.

The effective air gap  $Path4_b$  is further divided into 2 sections.  $Path4_{b1}$  is where opposing faces are horizontal and the magnetic flux through is vertical, therefore the magnetic reluctance of  $Path4_{b1}$  is:

$$R_{Path4_{b1}} = \frac{h_{\text{air}}}{\mu_0 r_{\text{cham}}^2 \pi} \tag{2.4}$$

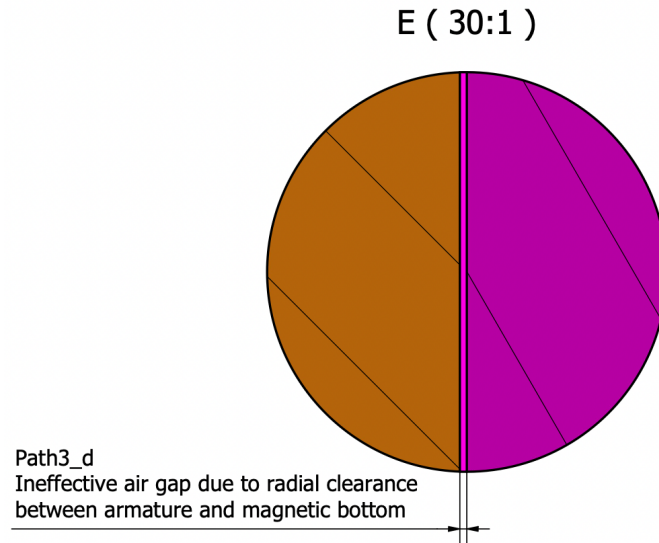


Figure 2.4: Detail view on horizontal air gap between magnetic bottom and armature.

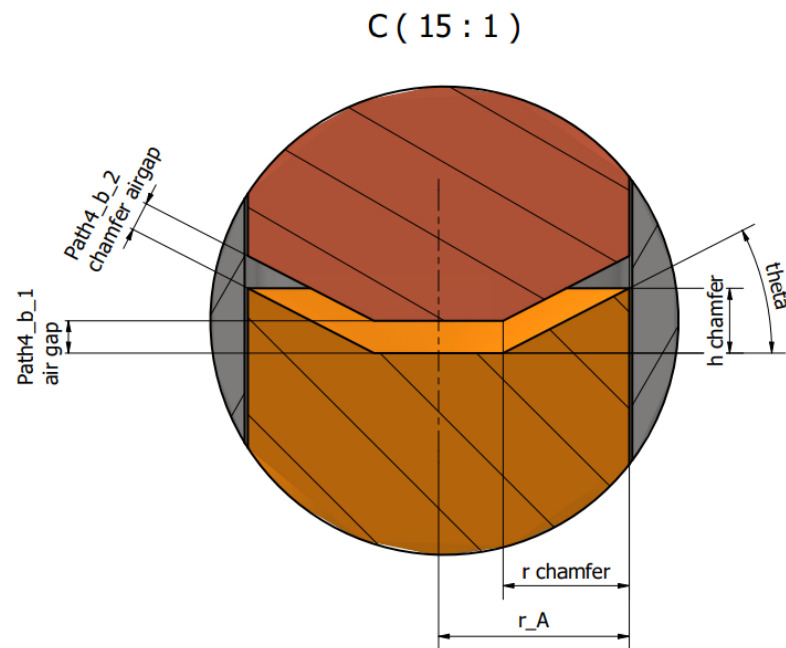


Figure 2.5: Detail view on vertical effective air gap between magnetic top and armature.



Computing  $Path4_{b1}$  is trickier. First we compute

$$\theta = \text{atan}\left(\frac{h_{\text{cham}}}{r_{\text{cham}}}\right) \quad (2.5)$$

$$h_{\text{chamferAirgap}} = h_{\text{air}} \cos(\theta) \quad (2.6)$$

and then we assumed that

$$A_{\text{chamfer}} = \pi (r_A^2 - (r_A - r_{\text{cham}})^2) \quad (2.7)$$

When we apply the eq. 1.3 we compute  $Path4_{b2}$  as the following:

$$R_{Path4_{b2}} = \frac{h_{\text{air}}}{\mu_0 \pi \left( \frac{h_{\text{cham}}^2}{r_{\text{cham}}^2} + 1 \right) (r_A^2 - (r_A - r_{\text{cham}})^2)} \quad (2.8)$$

Total effective reluctance  $Path4_b$  is computed with the following assumption for parallel magnetic flux in eq 2.9

$$\frac{1}{R_{\text{combined}}} = \frac{1}{R_1} + \frac{1}{R_2} + \dots + \frac{1}{R_n} \quad (2.9)$$

$$\frac{1}{R_{\text{combined}}} = \frac{1}{R_{Path4_{b1}}} + \frac{1}{R_{Path4_{b2}}} \quad (2.10)$$

$Path4_b$  is computed and simplified in eq. 2.11.

$$\begin{aligned} R_{\text{combined}} &= \frac{1}{\frac{1}{R_{Path4_{b1}}} + \frac{1}{R_{Path4_{b2}}}} \\ &= \frac{1}{\frac{\pi \mu_0 (r_A - r_{\text{cham}})^2}{h_{\text{air}}} - \frac{\pi \mu_0 \left( \frac{h_{\text{cham}}^2}{r_{\text{cham}}^2} + 1 \right) ((r_A - r_{\text{cham}})^2 - r_A^2)}{h_{\text{air}}}} \\ &= \frac{h_{\text{air}} r_{\text{cham}}}{\mu_0 \pi (2 h_{\text{cham}}^2 r_A - r_{\text{cham}} h_{\text{cham}}^2 + r_{\text{cham}} r_A^2)} \end{aligned} \quad (2.11)$$

$$\begin{aligned} R_{Path4} &= \frac{c_a + \frac{h_C}{2} - h_{\text{air}} + t_{\text{cfa}} + \frac{t_{\text{mba}}}{2}}{\mu \mu_0 r_A^2 \pi} + \\ &\quad \frac{h_{\text{air}} r_{\text{cham}}}{\mu_0 \pi (2 h_{\text{cham}}^2 r_A - r_{\text{cham}} h_{\text{cham}}^2 + r_{\text{cham}} r_A^2)} + \\ &\quad \frac{c_a + \frac{h_C}{2} + t_{\text{cfa}} + \frac{t_{\text{mta}}}{2}}{\mu \mu_0 r_A^2 \pi} \end{aligned} \quad (2.12)$$

$$R_{\text{total}} = R_{Path1} + R_{Path2} + R_{Path3} + R_{Path4} \quad (2.13)$$

After computing the total reluctance we can compute the magnetic flux using the eq. 1.2 and the magneto motive force using the eq. 1.1.

## Chapter 3

## DYNAMIC MODEL OF A SOLENOID VALVE

## 3.1 Mechanical Model

The only moving part in this direct acting solenoid part is the armature. The normally closed solenoid valve is turned on and off via applying a voltage on the solenoid leads that creates the magneto motive force and lets the fluid flow through. In fig. 3.1 we present the forces acting on the armature.  $F_{mm}$  is the magneto motive force,  $F_{airgap}$  is the force generated by the fluid pressure in the air gap on the top surface of the armature,  $F_{chamber}$  is the generated by the fluid pressure in the chamber on the bottom surface of the armature and  $F_{spring}$  is the force generated by the compression spring. This free body diagrams describes the dynamic behaviour of the valve.

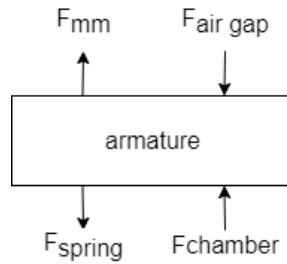


Figure 3.1: Armature Free Body Diagram

In section 2 we showed how to compute  $F_{mm}$  for a given design, armature position and applied current.

$$F_{mm} = \frac{1 \cdot \phi^2}{2 \cdot \mu_0 \cdot S_2} \quad (1.1)$$

$$F_{airgap} = \pi r_A^2 P_{airgap} \quad (3.1)$$

$$F_{chamber} = \pi r_A^2 P_{chamber} - \pi r_{orifice}^2 P_d \quad (3.2)$$

$$F_{spring} = (x + x_0) * k_s \quad (3.3)$$

where  $x_0$  stands for the pre-loading of the spring and  $k_s$  is the spring constant

$$F(t) = F_{mm}(t) - F_{airgap}(t) + F_{chamber}(t) - F_{spring}(t) \quad (3.4)$$

$$F(t) = m \ddot{x}(t) \quad (3.5)$$

$$\dot{x}(t) = \dot{x}(t-1) + \ddot{x}(t-1) dt \quad (3.6)$$

$$x(t) = x(t-1) + \dot{x}(t-1) dt + \ddot{x}(t-1) dt^2 \quad (3.7)$$

The mass of the armature can be computed from the material density (430F SS for this model)  $\rho$  and the armature geometry.

$$m = r_A^2 \rho \left( \frac{h_C}{2} + t_{cfa} \right) \quad (3.8)$$

### 3.2 Electrical Model

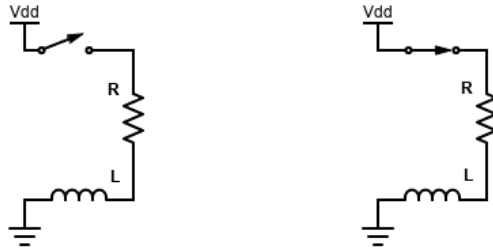


Figure 3.2: Schematic of electrical circuit. (left) Valve powered off. (right) Valve powered on.

In fig. 3.2 the electrical schematic of the valve is presented. A solid state relay (SSR) is used to switch the solenoid on and off and any losses due to wiring and SSR is ignored in the model. We can represent the schematic with the following equations:

$$\begin{aligned} V_{dd} &= V_L + V_R \\ &= L di + R i \end{aligned} \quad (3.9)$$

$$V_{dd} = L(t) \frac{di}{dt}(t) + R i(t) \quad (3.10)$$

Assuming  $V_{dd}$  is constant we can compute  $\frac{di}{dt}$  with the following derivation:

$$V_L(t) = V_{dd} - R i(t) \quad (3.11)$$

$$\frac{di}{dt}(t) = \frac{V_L(t)}{L(t)} \quad (3.12)$$

We can compute the inductance of the solenoid system using the eq. 3.13. Inductance will play a crucial role in the dynamic analysis of the solenoid valve. Inductance will dictate the reaction time of the solenoid valve.

$$L = \frac{N \phi}{i} = \frac{N^2}{R_{total}} \quad (3.13)$$

We can compute the resistance  $R$  from coil geometry ( $R_{Cin}$  coil inner radius,  $R_{Cout}$  coil outer radius), winding number  $N$ , wire diameter  $d_w$  and electrical resistivity of the conductor  $\rho$  as follows:

$$R = \pi (r_{Cout} + r_{Cin}) N \rho \quad (3.14)$$

Finally we can compute  $i(t)$  with the following equation:

$$i(t) = i(t-1) + \frac{di}{dt}(t-1) dt \quad (3.15)$$

Notice in fig. 3.2 that the circuit is a LR circuit. Valve reaction time is an important performance metric for solenoid valves. Generally it is assumed that  $3\tau$  is the time that the valve is fully opened. Valve closing time on the other hand depends on the spring constant  $k_s$  and pressure balance between chamber and air gap. This will be discussed in the next section.

$$\tau = \frac{L}{R} \quad (3.16)$$

Notice in eq. 3.13 inductance varies with magnetic flux, thus varies by  $R_{total}$ . This results in different time constants for different armature positions. For this dynamic model, a positive voltage will be applied for  $4\tau_{opening}$  seconds. After this duration the voltage will be removed and the simulation will be run for another  $4\tau_{closing}$  seconds.

$$\tau_{opening} = \frac{L(h_{air})}{R} \quad (3.17)$$

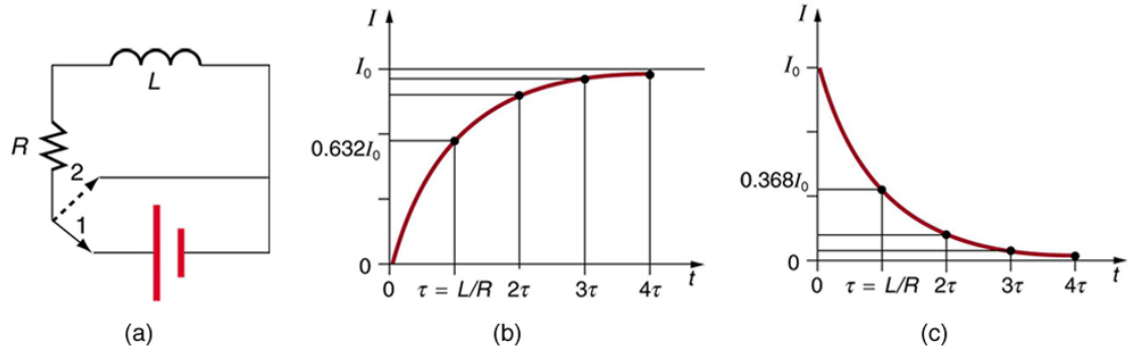


Figure 3.3: (a) An RL circuit with a switch to turn current on and off. When in position 1, the battery, resistor, and inductor are in series and a current is established. In position 2, the battery is removed and the current eventually stops because of energy loss in the resistor. (b) A graph of current growth versus time when the switch is moved to position 1. (c) A graph of current decay when the switch is moved to position 2.[OpenStax, 2022]

$$\tau_{closing} = \frac{L(c_a)}{R} \quad (3.18)$$

In eq. 3.17 the inductance is computed with the maximum air gap and in eq. 3.18 the inductance is computed with minimum air gap that is equal to the axial clearance  $c_a$ .

### 3.3 Simulation Meta Data

Simulation time step is set to  $1\mu s$ ,  $10^{-6}s$ , in order to account for the dynamic nature of the simulation. As it is presented in the next section, mass flows and the change in pressures and temperatures are integrated through the simulation. A small time step is required to keep the simulation stable. For step sizes above  $1\mu s$  the simulation diverges due to small control volumes and high flow rates.

### 3.4 Flow Model

The valve design has 2 control volumes. These control volumes are  $V_{airgap}$  and  $V_{chamber}$ . The states of these volumes are defined by their volume  $V$ , temperature  $T$ , density  $\rho$  and mass  $M$ . The interaction between these control volumes are defined by the armature radial clearance flow path. This flow path is defined by a flow cross

section area  $A_{rc}$  and a discharge coefficient  $C_{d,rc}$ .

The valve is placed between two reservoirs, upstream and downstream. For this model the upstream and downstream reservoirs are assumed to be infinite and have constant temperature and density. The interaction between the chamber and the reservoirs are defined by inlet and outlet orifices. These orifices are defined by  $r_{inlet}$ ,  $C_{d,inlet}$ ,  $r_{outlet}$  and  $C_{d,outlet}$ . Outlet orifice is open gradually due to the mechanics of the armature. This is taken in to account by multiplying the effective area with the armature travel percentage.

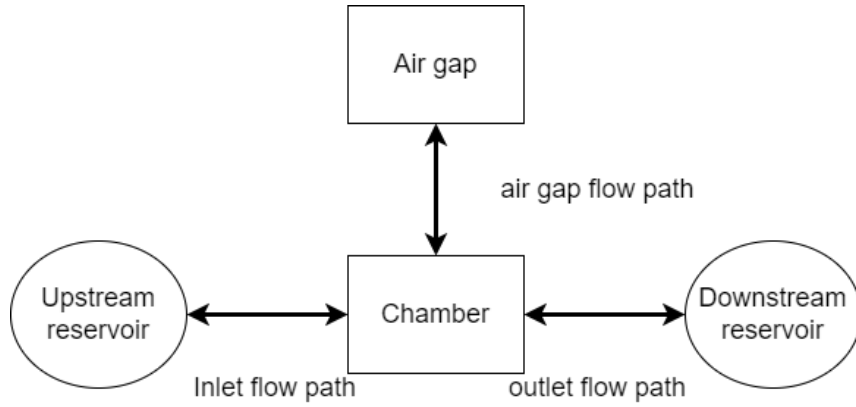


Figure 3.4: Abstraction of valve volumes, and flow paths.

The following subsections will present the simulation algorithm in the order of execution for each loop.

#### 3.4.1 Armature Motion

The armature motion is computed with the forces computed in the previous loop with order: eqs. 3.5, 3.6, 3.7. After computing this loops position, velocity and acceleration; if they exceed the range of motion position is capped and velocity and acceleration is set to zero.

#### 3.4.2 Electrical and Magnetic Circuit Simulation

The electrical current for this loop is computed with eq. 3.15. The applied voltage is calculate based on the time in the simulation mentioned in eqs 3.17 and 3.18.  $R_{total}$

is computed with the current armature position and used to calculate current flux with eq. 1.2.  $F_{mm}$  is computed with eq. 1.1. Inductance voltage  $V_L$  and change in electrical current for next step  $\frac{di}{dt}$  is computed with eqs. 3.11 and 3.12.

### 3.4.3 Control Volume Changes

Volume of the air gap and the chamber changes due to armature translation. This changes the temperature and the pressure in these control volumes. These processes are assumed to be adiabatic compression/expansion because the volume changes happen under in the order of  $us$ .

$$P(i) = P(i-1) \left( \frac{V(i-1)}{V(i)} \right)^\gamma \quad (3.19)$$

$$T(i) = T(i-1) \left( \frac{V(i-1)}{V(i)} \right)^{(\gamma-1)} \quad (3.20)$$

### 3.4.4 Gas Flows

It is assumed that the flow velocities at the inlet, outlet and the radial clearance around the armature are normal to the flow restriction surfaces. It is also assumed that all intensive properties (specific internal energy, specific volume, specific enthalpy, temperature, pressure and specific entropy) are uniform over the flow restriction surfaces, thus the flow is assumed to be 1D.

The order of gas flow computation is from downstream to upstream. First the mass flow from chamber to downstream reservoir  $\dot{m}_{c,d}$  and its effects on the  $M_{chamber}$ ,  $P_{chamber}$  and  $T_{chamber}$  are computed. Then the mass flow between chamber and air gap  $\dot{m}_{c,a}$  and its effects on  $M_{chamber}$ ,  $P_{chamber}$ ,  $T_{chamber}$ ,  $M_{airgap}$ ,  $P_{airgap}$  and  $T_{airgap}$  are computed. Finally the mass flow from upstream reservoir to chamber  $\dot{m}_{u,c}$  and its effects on the  $M_{chamber}$ ,  $P_{chamber}$  and  $T_{chamber}$  are computed.

### Computing Flow Velocity

$$M = \sqrt{\left( \frac{P_{high}}{P_{low}} \right)^{\left( \frac{\gamma-1}{\gamma} \right)} \frac{2}{\gamma-1}} \quad (3.21)$$

Flow velocity between two pressure reservoirs is computed by the eq. 3.21 derived from the adiabatic flow equation [NASA, 2021]. If the resulting Mach number  $M$  is greater than 1, it is capped to 1 because the flow through orifices is choked.

#### *Computing Mass Flow Rate*

After computing flow velocity  $M$  one can compute the mass flow rate  $\dot{m}$  using the eq. 3.22 [NASA, 2021], where  $A$  is the orifice surface area,  $P_t$  is the total/upstream pressure,  $T_t$  is the total/upstream temperature,  $R$  is the gas constant,  $\gamma$  is the ratio of specific heats for the gas and  $C_d$  is the discharge coefficient for the given flow restriction area.

$$\dot{m} = C_d \frac{A P_t}{\sqrt{T_t}} \sqrt{\frac{\gamma}{R}} M \left( 1 + \frac{\gamma - 1}{2} M^2 \right)^{-\frac{\gamma + 1}{2(\gamma - 1)}} \quad (3.22)$$

#### *Computing Gas Charge/Discharge*

After computing the mass flow rate  $\dot{m}$  between two control volumes/reservoirs, the new mass  $M$ , pressure  $P$  and temperature  $T$  should be computed for the control volumes.

$$\Delta m = \dot{m} dt = M(i) - M(i - 1) \quad (3.23)$$

$$M(i) = M(i - 1) + \Delta m \quad (3.24)$$

To compute the next state of the control volumes it is assumed that the process is adiabatic. Thus we can write the following energy and mass conservation.

$$\Delta m = M(i) - M(i - 1) \quad (3.25)$$

$$\Delta e = U(i) - U(i - 1) = H \quad (3.26)$$

$$\Delta e = M(i) u(i) - M(i - 1) u(i - 1) = \Delta m h \quad (3.27)$$

$$0 = \Delta m h - M(i) u(i) + M(i - 1) u(i - 1) \quad (3.28)$$

$$0 = \Delta m P v - M(i) C_v T(i) + M(i - 1) C_v T(i - 1)$$



Eq. 3.28 leverages the fact that work done by entering/exiting gas can be computed using its enthalpy to simplify the expression.

$$T(i) = \frac{U(i)}{M(i) C_v} \quad (3.29)$$

$$P(i) = \frac{RT(i)}{v} \quad (3.30)$$

Control volume states are computed with the equations above with the ideal gas assumptions.

### *Computing Forces on Armature*

Last step of the simulation loop is to compute the forces acting on the armature. These forces are computed with the eqs. 1.1, 3.1, 3.2, 3.3 and 3.4. After computing the net force one can compute the dynamic behavior of the armature using eqs. 3.5, 3.6 and 3.7.

## Chapter 4

**SIMULATION**

Using the model described in the previous chapter we ran the simulation with a time step of  $1\mu$  seconds.

Simulation is set with the following parameters:

$$c_r = 0.05mm$$

$$c_a = 0.05mm$$

$$h_C = 25mm$$

$$r_{Cout} = 12mm$$

$$D_w = 0.27mm$$

$$t_{cfr} = 1.5mm$$

$$t_{cfa} = 3mm$$

$$t_{mba} = 1mm$$

$$t_{mta} = 1mm$$

$$r_A = 3.95mm$$

$$r_{cham} = 2mm$$

$$h_{cham} = 2mm$$

$$t_{shell} = 2mm$$

$$PR = 1$$

$$CSF = 0.9$$

$$h_{air} = 0.5mm$$

$$\mu_r = 550$$

$$\mu_0 = 1.25663706212 \cdot 10^{-6} H/m$$

$$CWCC = 10 \cdot 10^6 A/m^2$$

$$erc = 1.68 \cdot 10^{-8} \Omega m$$

$$t_{powered on} = 4 \tau_{open}$$

$$t_{powered off} = 4 \tau_{close}$$

$$P_u = 50bar$$

$$P_d = 1bar$$

$$T_u = T_d = 273K$$

$$K_{spring} = 25N/mm$$

$$x_{preload} = 0.5mm$$

The parameters given above define other properties of the solenoid valve. Total number of winding turns  $N$  is set to 2229. Total length of the conductor is set to 122.5m. Resistance of the conductor is set to  $36\Omega$ . Maximum current allowed on the circuit is set to 0.5A. The ampere-turns is set to 1149A. The voltage applied to drive the circuit is set to 18.5V. Maximum magnetic field strength that will be reached at peak current is set to  $46kA/m$ . The solenoid time constants are set to  $\tau_{open} = 10.9\mu s$  and  $\tau_{close} = 15.5\mu s$ .

Another important property of the valve is the outlet orifice area. Outlet orifice area has two effects on the valve. First, it limits the maximum flow rate. Second, when the valve is closed the area over the outlet orifice is sealed and there is a pressure differential that results in a net force. As the orifice area increases so does this force, which results in higher  $F_{mag}$  requirements. There is a relation between outlet orifice area and the armature range of motion due to flow restriction area.

$$\begin{aligned} \pi 2 r_{outlet} h_{airgap} &= \pi r_{outlet}^2 \\ 2 h_{airgap} &= r_{outlet} \end{aligned} \tag{4.1}$$

The side surface of the cylinder that has the same radius with the outlet orifice and the height of the air gap should be equal to the surface area of the outlet orifice for optimal flow rate and  $F_{mag}$ .

The driving force of this simulation is the effects of the magnetic field generated by the coil. In fig. 4.1, one can observe the change in magnetic flux density with the current applied to the circuit. Note that magnetic flux tapers off while current increases further. This is because of the magnetic saturation simulated using the materials B-H curve. The effect of this saturation can be seen in fig. 4.2.

The magnetic field density increases linearly with the magnetic field strength until the solenoid generates enough force and pulls the armature. When the armature

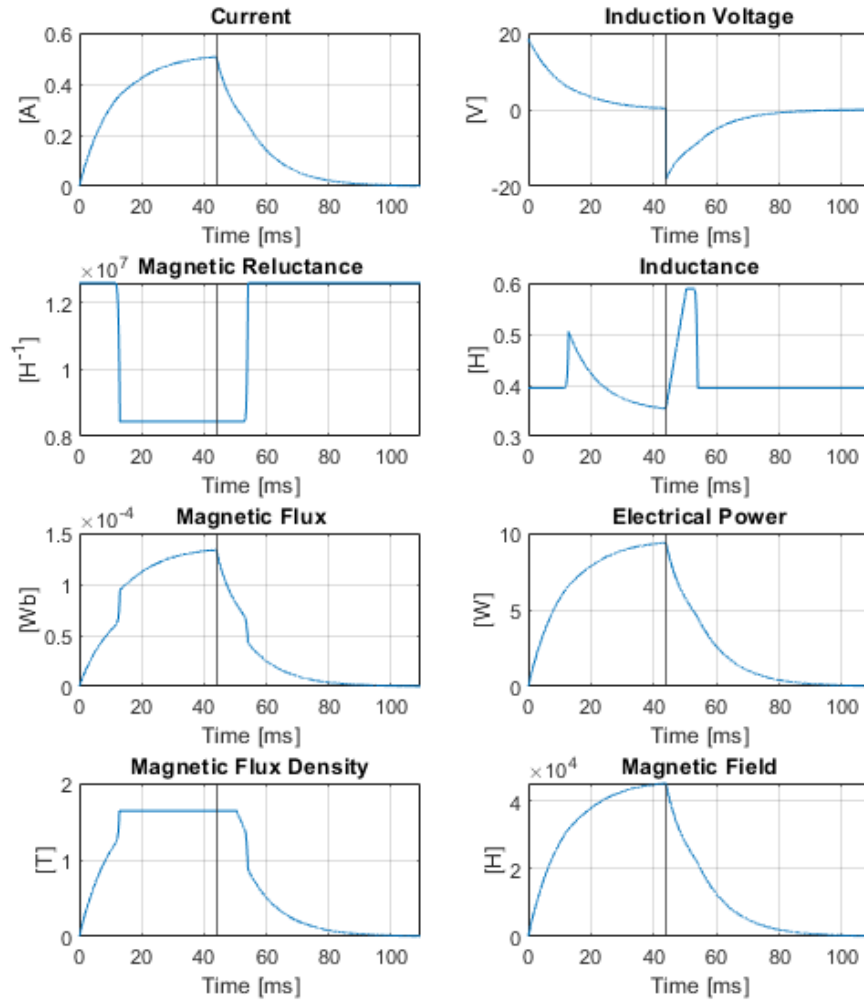


Figure 4.1: Electrical and magnetic circuit development over time.

is fully retracted, the total magnetic reluctance in the circuit diminishes because the effective air gap used to dominate the total reluctance in the magnetic circuit is now filled with 430f SS. After the armature is fully retracted, initially the manufacturing tolerances and clearances start to dominate the total magnetic reluctance but, with increasing magnetic field strength the magnetic permeability of the 430f SS starts to taper off and eventually gets closer to the magnetic permeability of free space  $\mu_0$ . This limits the maximum force that can be generated with the given design.

The magneto motive force,  $F_{mag}$ , generated tips the force balance on the arma-

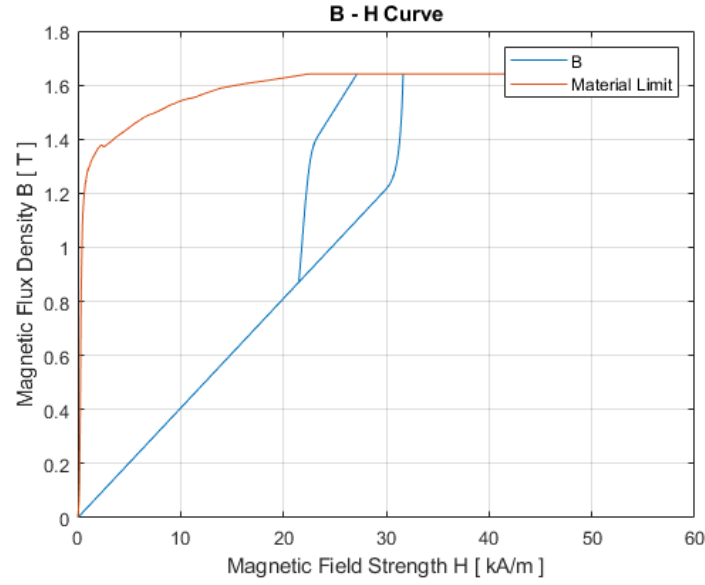


Figure 4.2: Magnetic field strengths and magnetic flux densities reached during simulation.

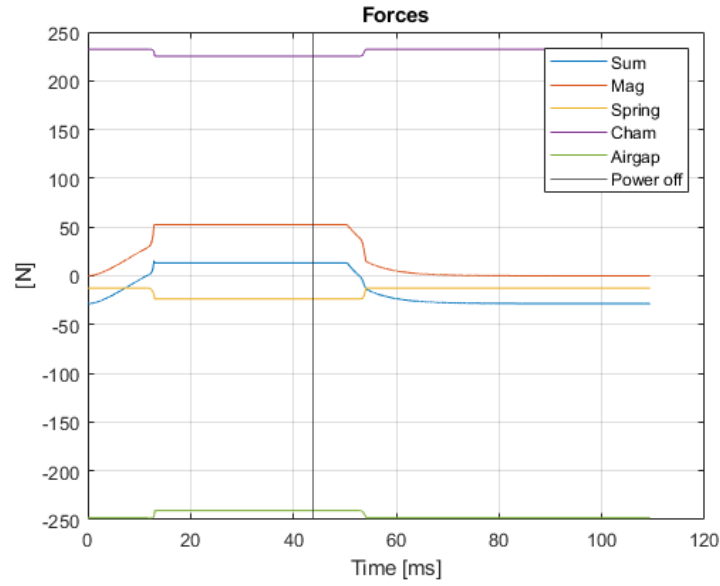


Figure 4.3: All forces acting on the armature.

ture and causes it to retract. In fig. 4.3 all the forces acting on the armature are presented. Notice that magnetic force linearly increases with the applied current until it overcomes the spring and pressure forces. Once the armature starts to retract, the  $F_{mag}$  increases exponentially until it is tapered off due to magnetic flux

tapering off. This exponential rise and tapering off can be better seen in fig. 4.4.

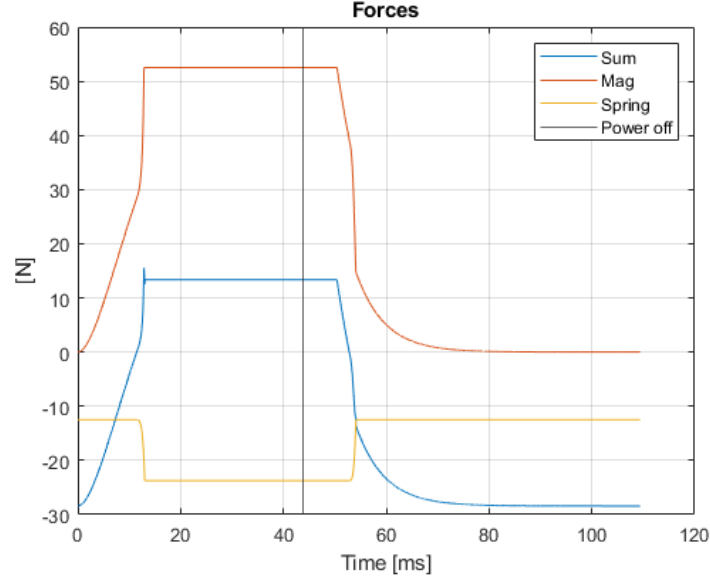


Figure 4.4: Forces acting on the armature excluding pressure forces.

Notice the black vertical line on the plot, it represents the moment the applied voltage is removed. Notice that it takes a considerable amount of time to  $F_{mag}$  to diminish. We will further explore this when optimizing the valve to react faster.

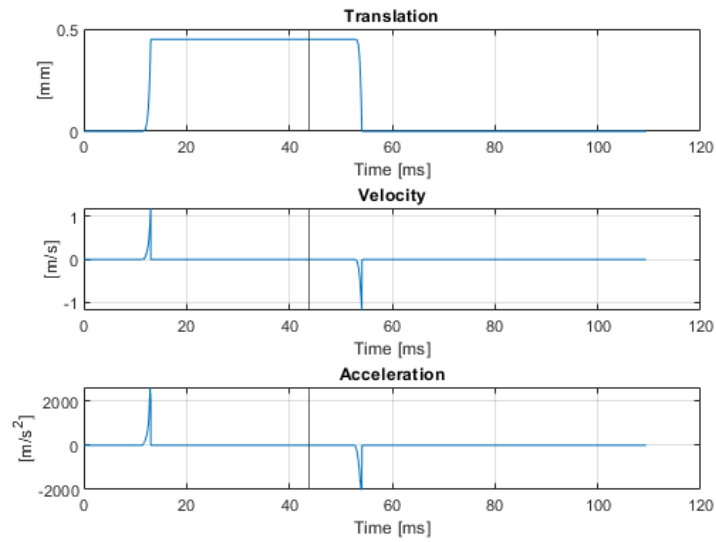


Figure 4.5: Motion on the armature.

In fig. 4.5, the kinematics of the armature are presented. Notice that the actual motion takes a very small time compared to the magnetic field building up or the gas exchange between two chambers.

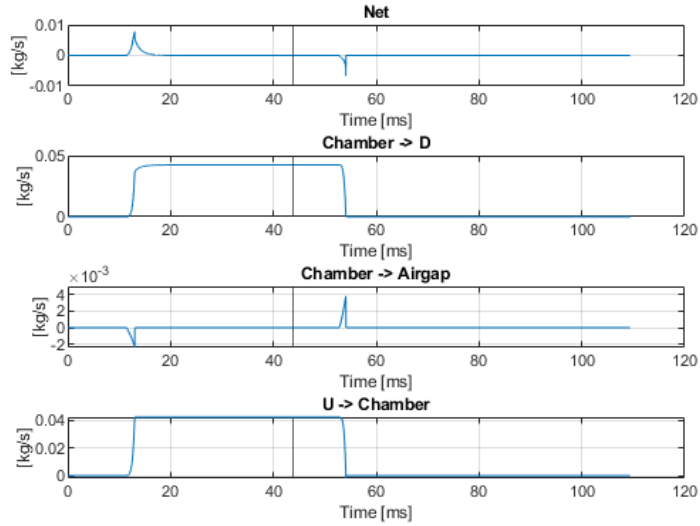


Figure 4.6: Mass flows to and from control volumes.

In fig. 4.6, the effect of armature movement is presented, gas flows from the upstream reservoir to the downstream reservoir through the chamber. Due to armature movement, volumes of the air gap and the chamber changes, this can be seen in fig. 4.9 and 4.10. In this simulation all thermodynamic processes are assumed to be adiabatic, the effect of this assumption can be seen in the rising temperature of the compressed volume. The reverse of same effect is in place in the expanding volume.

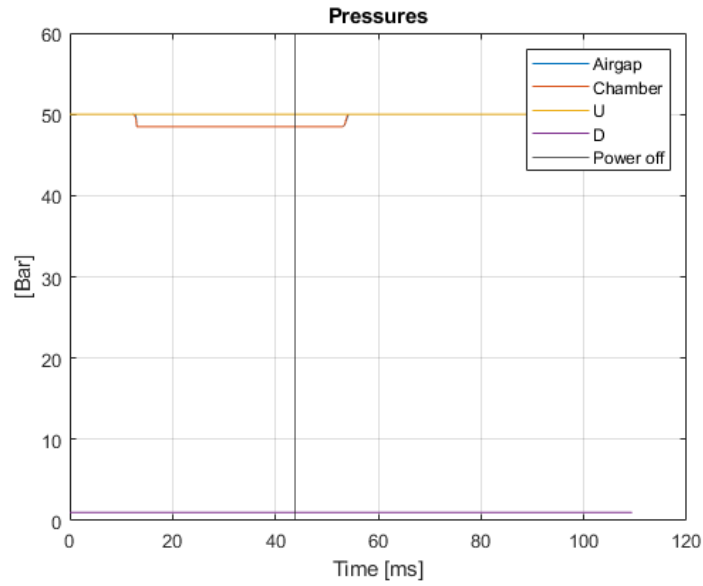


Figure 4.7: Pressures of control volumes and reservoirs.

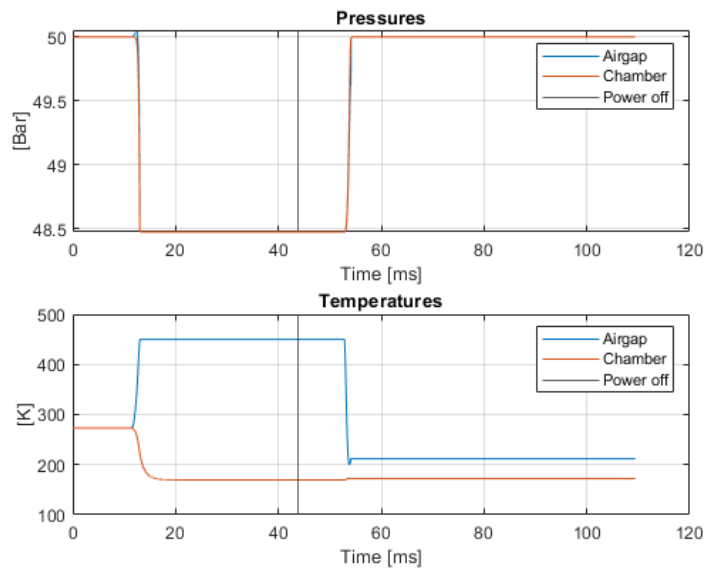


Figure 4.8: Control volume pressure and temperature



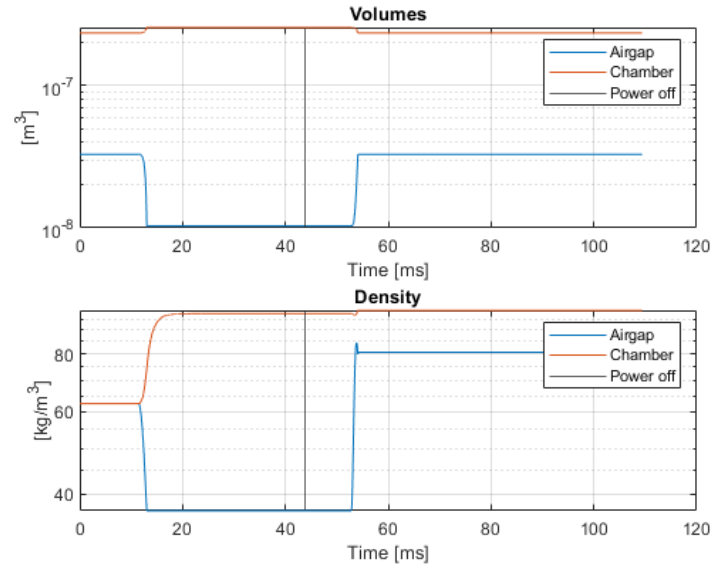


Figure 4.9: Change of the volumes

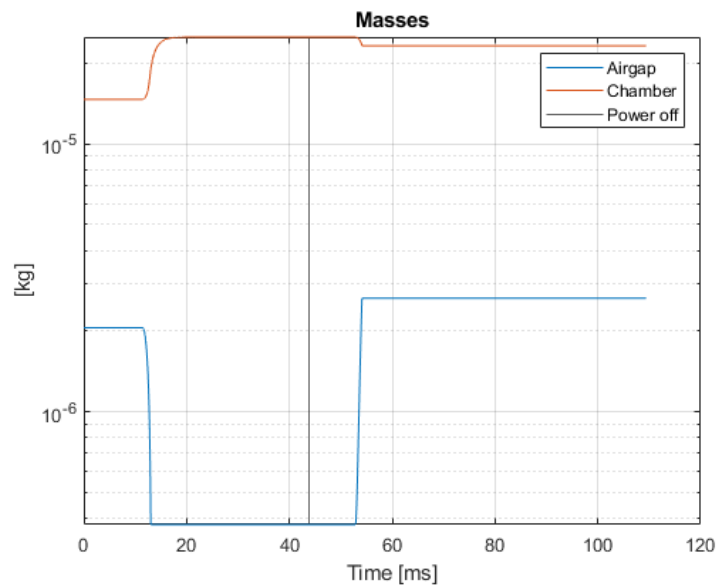


Figure 4.10: Change of the masses

## Chapter 5

### CONCLUSION

In aerospace application there are various uses for solenoid valves. Other than simply be used as valves, in space systems they are used for attitude control thrusters and in rocket applications they can be used as bang-bang pressure regulators. When designing a valve, the weight, the opening time, closing time and power required to operate are important parameters. These parameters should be optimized simultaneously but often there are no single solution which optimized all these parameters at once. Thus, it is important to search the design option space efficiently and account for manufacturing tolerances.

The simulation results presented in the previous chapter is obtained by using the optimized parameters which resulted from multi objective optimization process. Since there are 15 parameters and the permutation of 2 options for each would take  $2^{15}$  iterations, the valve was optimized step by step.

The simulation was also run short to focus on opening and closing events. The driving voltage is applied until the armature is fully retracted. After that the driving voltage was removed and the simulation continued until the armature reached its initial position.

#### 5.1 Optimizing Coil Parameters

There are 3 parameters that dominate coil design and the search space for these were as follows:

$$r_{cout} = 12 : 2 : 20 \text{ mm}$$

$$h_C = 25 : 10 : 75 \text{ mm}$$

$$r_A = 3 : 1 : 5 \text{ mm}$$

After running the simulation there are 3 designs of interest, these are the fastest

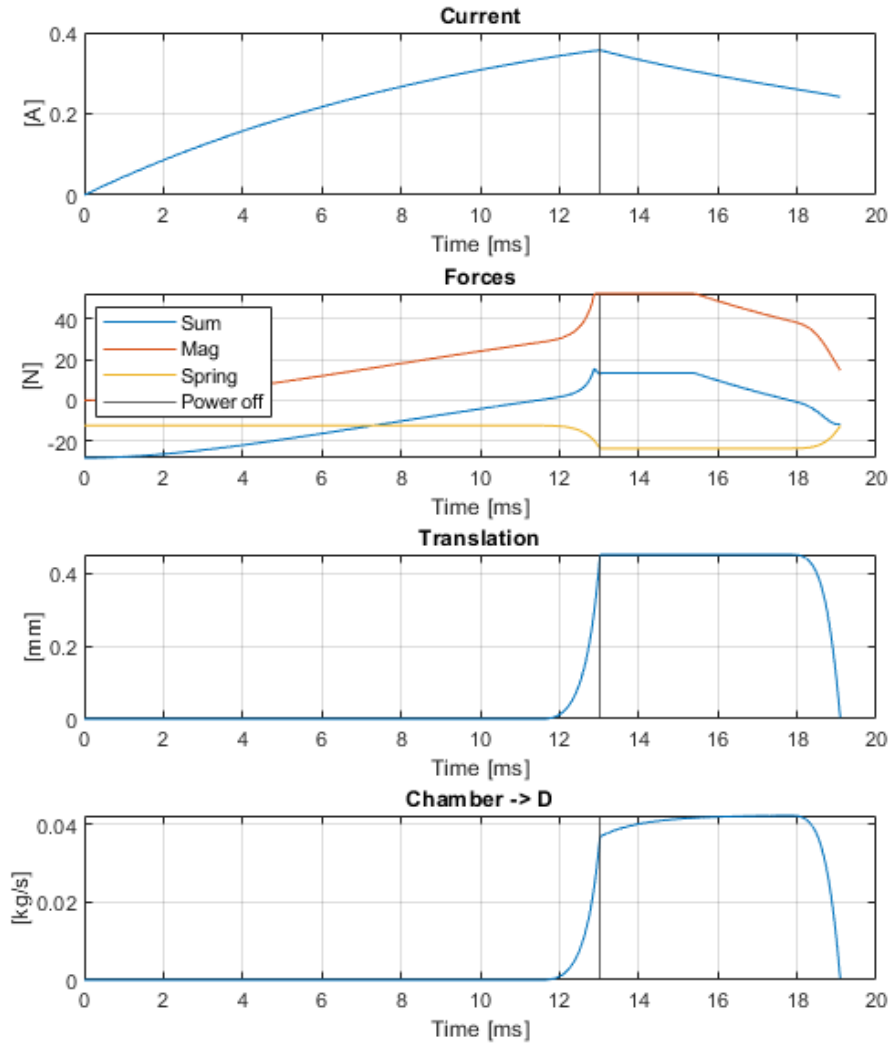


Figure 5.1: Shortened simulation visualization. Simulation and driving voltage start at  $t = 0$ , and driving voltage is removed at the vertical black line.

overall, the one with the minimum mass flow per cycle and the one with the maximum flow rate in oscillating mode. The fig. 5.2 presents us a trade-off between opening and closing time of the valve.

Since the gas flow only occurs when the valve is open and the retraction of the armature takes a fraction of time it is no surprise that the minimum flow per cycle is achieved with the design that has the shortest closing time of them all.

For the maximum flow rate in oscillating mode, the opening time is critical since a reduction in opening time will reduce the time when the valve is in closed position. Therefore the maximum flow rate in oscillating mode is achieved by a design which has one of the fastest opening time and one of the slowest closing time.

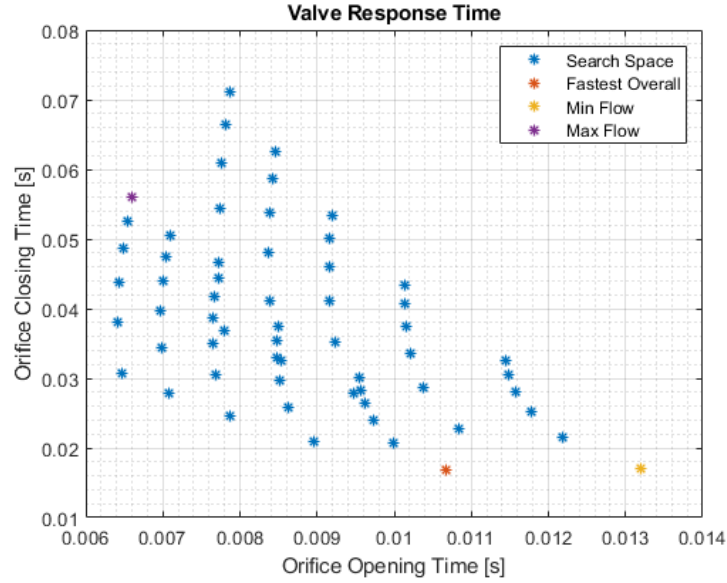


Figure 5.2: Response times of various design options. Trade-offs between opening and closing times.

The fig. 5.3 presents us the trade-off between valve weight and the maximum flow rate in oscillating mode. When picking reaction control thrusters there is trade-off between thruster frequency and its weight.

However for a bang-bang regulator the most crucial parameter of a solenoid valve is its closing time/minimum flow. With decreasing minimum flow, the system can be more responsive and precise. Fortunately for us, in our optimization we found that there is not a trade-off between valve weight and its minimum flow capacity as seen in fig. 5.4. The valve with the fastest response was picked and is used in the next optimization steps.

$$r_{cout} = 12 \text{ mm}$$

$$h_C = 25 \text{ mm}$$

$$r_A = 4 \text{ mm}$$

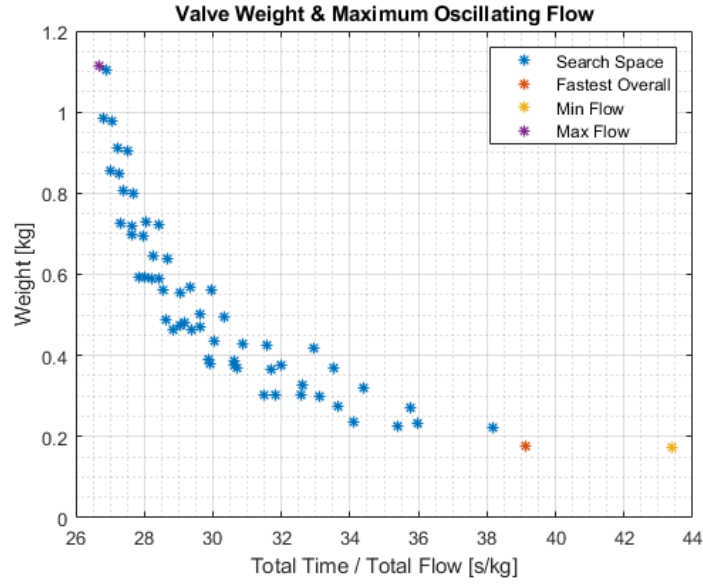


Figure 5.3: x axis represents the time it takes to flow 1 kg of gas during an oscillating valve operation (continuous opening and closing of the valve).

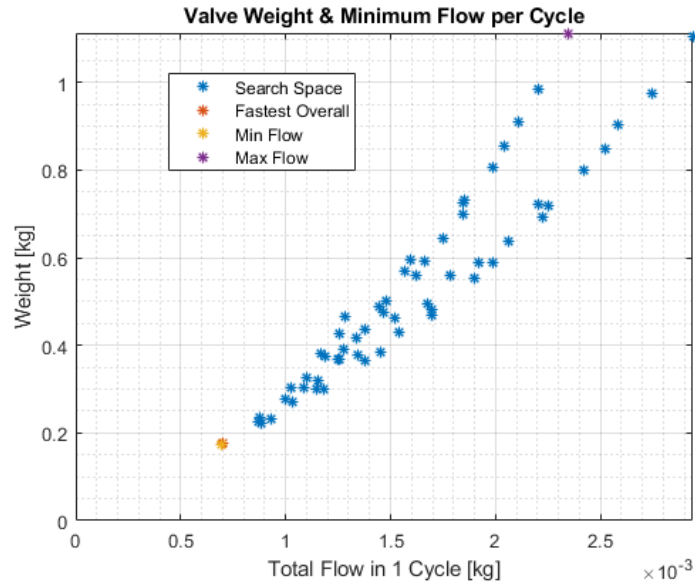


Figure 5.4: Results of simulation: Valve Weight and minimum flow per cycle

## 5.2 The Effect of Structural Elements Thickness

After finding the optimal coil parameters, it is time to look into structural parameters and their effects on weight and minimum mass flow per cycle. There are 5

parameters that can be considered as structural elements these were as follows:

$$t_{cfr} = 1 : 0.1 : 1.5 \text{ mm}$$

$$t_{cfa} = 3 : 1 : 5 \text{ mm}$$

$$t_{mba} = 1 : 1 : 5 \text{ mm}$$

$$t_{mta} = 1 : 1 : 5 \text{ mm}$$

$$t_{shell} = 1 : 1 : 2 \text{ mm}$$

A total of 216 designs were simulated.

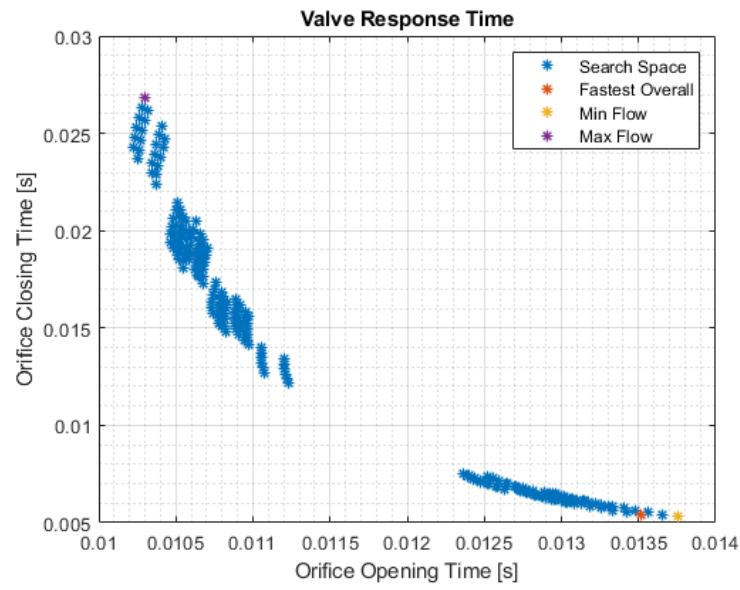


Figure 5.5: Response times of various design options. Trade-offs between opening and closing times.

Similar to the coil parameter results we see the trade-off between valve opening and closing time. The fastest option is picked for further clearance analysis:

$$t_{cfr} = 1.5 \text{ mm}$$

$$t_{cfa} = 3 \text{ mm}$$

$$t_{mba} = 1 \text{ mm}$$

$$t_{mta} = 1 \text{ mm}$$

$$t_{shell} = 1 \text{ mm}$$

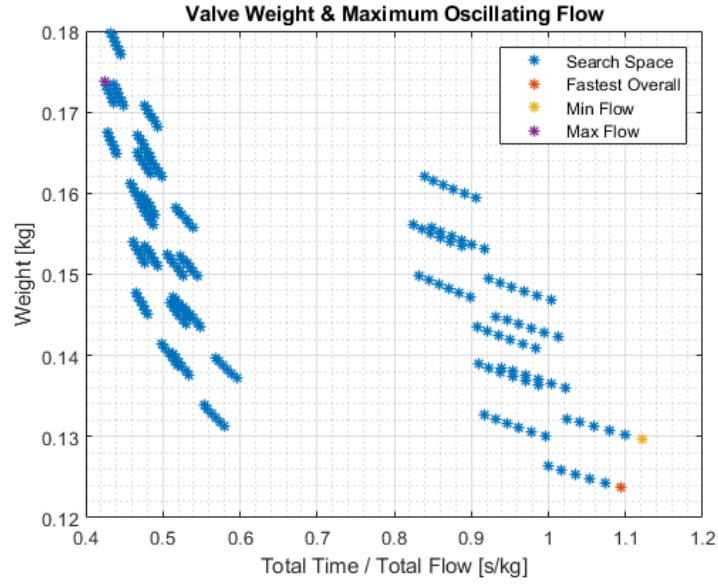


Figure 5.6: x axis represents the time it takes to flow 1 kg of gas during an oscillating valve operation (continuous opening and closing of the valve).

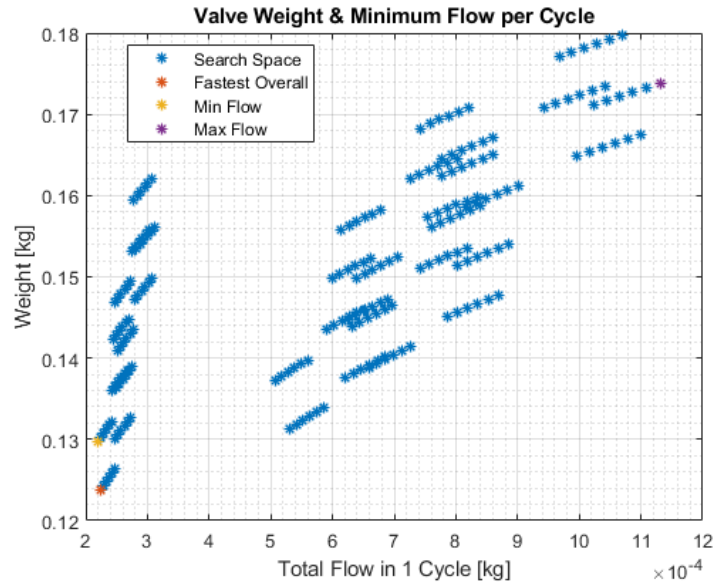


Figure 5.7: Results of simulation: Valve Weight and minimum flow per cycle

### 5.3 The Effect of Clearances and Tolerances

It is time to look into clearances, tolearances and their effects on weight and minimum mass flow per cycle. There are 5 parameters that can be considered as struc-

tural elements these were as follows:

$$c_a = 0.05 : 0.0.02 : 0.09 \text{ mm}$$

$$c_r = 0.05 : 0.0.02 : 0.09 \text{ mm}$$

A total of 9 designs were simulated.

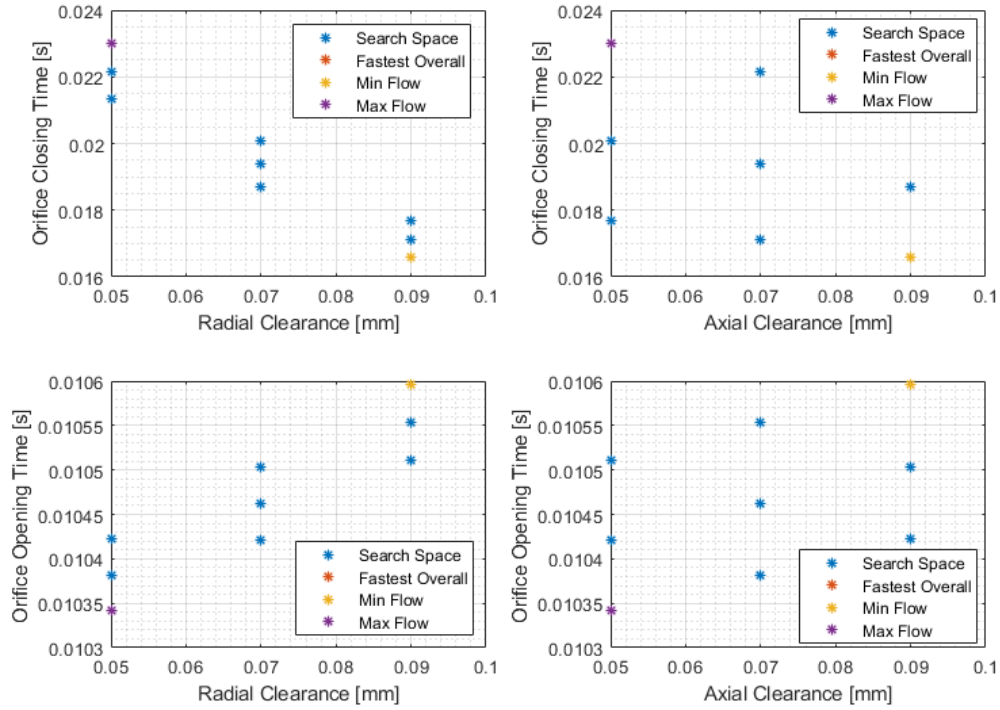


Figure 5.8: The effect of clearances on valve opening and closing times.

As seen in fig. 5.8, radial and axial clearance is directly proportional with orifice opening time and inversely proportional with orifice closing time. It should be noted though the radial clearance has a much higher impact than the axial clearance. This is because as radial clearance increases the armature surface area decreases and the coil turns decreases.

While axial clearance has almost no effect on weight, radial clearance has a minimal effect due to reduced number of turns and reduced armature surface area.

The final design is presented in fig. 5.10. Final design can be compared with the initial design of reference in fig. 2.1. Notice that the optimization was only done on magnetic circuit elements. The structural casing, valve seat and seal was omitted



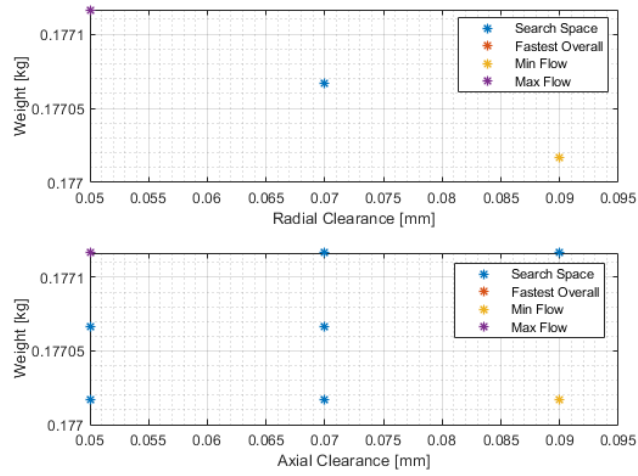


Figure 5.9: The effect of clearances on valve weight.

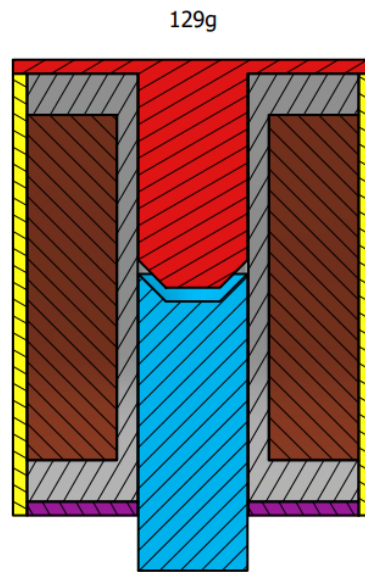


Figure 5.10: The 3D model of the optimized valve.

for the computation because it is assumed that the smaller solenoid and magnetic circuit design will lead to the smallest overall design. With the addition of valve seat, casing and seal the resulting valve should not exceed 200g in weight.

## BIBLIOGRAPHY

[NASA, 2021] NASA (2021). Isentropic flow equations.

[OpenStax, 2022] OpenStax (2022). 23.1: Rl circuits. *Physics LibreTexts*.

[Yang et al., 2019] Yang, M., Zhang, J., Bing, X., and Wang, W. (2019). Study on electromagnetic force of the new micro digital valve. *Microsystem Technologies*, 25.

[Zhao et al., 2017] Zhao, J., Shi, Y., Grekhov, L., and Ma, X. (2017). Effects of structure parameters on the static electromagnetic characteristics of high speed solenoid valves. *International Journal of Applied Electromagnetics and Mechanics*, 55:1–16.

## Appendix A

Source code: <https://github.com/khanliKU/thesis>